Structural Dynamics for Aeroelastic Analysis

João Daniel dos Santos Almeida
joao.s.almeida@ist.utl.pt

Instituto Superior Técnico, Lisboa, Portugal

November 2015

Abstract

Aeroelasticity is a physical phenomenon resulting from the interaction of aerodynamic, elastic and inertial forces. It is very important to study aeroelasticity in aircraft structures, due to their lightweight and flexible design. The present work aims to study the aeroelastic behavior of a 3D aircraft wing. For that, a beam representation of the wing structure is developed using the finite-element method. The one-dimensional beam coincides with the wing elastic axis with the whole rigidity of the wing concentrated along it. Therefore, a new computational aeroelasticity framework was created using the structural model developed and integrating an available fluid solver, which uses a panel method to solve the fluid. Both the fluid and structural solvers are validated with published results. The coupling of the two domains is made using an adequate time discretization scheme, which is chosen after performing several analyses using different temporal schemes. The framework is validated with available trim results from a wing model. The results are then presented for a wing denoted as reference case. A parametric study is conducted and its results compared with the reference values. It is concluded that the results show very good agreement with the theoretical expectations. Moreover, an aero-structural optimization of a wing is tackled aiming to minimize its total mass while fixing the lift coefficient. Despite the many simplifications implemented in both the fluid and structural solvers, this framework proves to be useful to predict the aeroelastic performance of a wing in the early stages of aircraft design.

Keywords: Aeroelasticity, Panel method, Finite element method, Fluid-structure interaction, Coupling schemes, Flutter

1. Introduction

The science of aeroelasticity is of the most importance in aircraft design. According to [1], aeroelasticity can be defined in the following manner:

"Aeroelasticity is concerned with those physical phenomena which involve significant mutual interaction among inertial, elastic and aerodynamic forces".

Since the primordials of the aviation history, it has been proved that to mitigate the adverse effects of aeroelasticity, aircraft should have a structure capable of withstanding the several loads encountered in each flight while favoring mass distribution. Nowadays, in order to prevent the negative consequences of aeroelasticity and to better understand and control it, several computational aeroelastic tests can be performed in early stages of aircraft design, posing as efficient and accurate methods and lowering the number of experimental tests needed.

To better visualize the context of aeroelasticity, a triangle is used, presented in Figure 1. This triangle represents the three main disciplines directly related to dynamic aeroelasticity. By pairing two corners of the triangle, one can identify other important technical fields posing as special aspects of aeroelasticity. For instance:

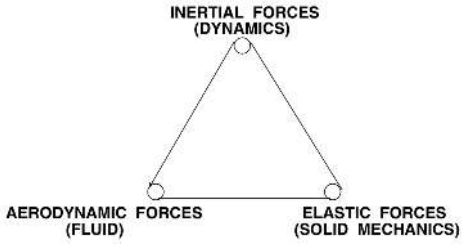

Figure 1: Collar diagram, adapted from [1].

- *Stability and control (flight mechanics)* = inertial forces + aerodynamic forces;
- *Structural vibrations* = inertial forces + elastic forces;
- *Static aeroelasticity* = aerodynamic forces + elastic forces.

The most common static aeroelastic problem is the torsional divergence of a wing, which occurs when the torsional moment resulting from aerodynamic forces outbalances the torsional rigidity of the wing. On the other hand, flutter is considered to be the most dangerous dynamic problem. It is a self-excited oscillatory instability in which aerodynamic forces couple with the natural modes of vibration of a elastic body, producing vibrations with increasing amplitude.

Two main objectives support this work. The first main objective is to develop a dynamic structural model for the wing, representing it as an equivalent beam, in order to be used in an aeroelastic framework, applying the finite element method and taking into account the mass and stiffness matrices of the system. The second main objective is to benchmark and study several implemented coupling methods, which are used to couple the fluid and structural domains, concluding about the accuracy, stability and efficiency of those methods and perform a parametric study with one of these methods to study the impact of several variables on the wing flapping motion.

2. Fluid Dynamics Model

To compute the aerodynamic forces, an existing fluid solver tool is used and adapted to this work, which is mathematically based on potential flow theory.

2.1. Potential Flow

The potential flow model is a formulation in which the flow is assumed to be inviscid, irrotational and isentropic. Compressible effects are out of the scope of this thesis, so the fluid is also assumed incompressible. However, it is found acceptable for this framework because the airspeed is in the subsonic domain and no shocks nor separation effects are expected. As a result, the governing equation is

$$\nabla \cdot \vec{V} = \nabla \cdot (\nabla \phi) = \nabla^2 \phi = 0\,, \tag{1}$$

where $\phi(x, y, z)$ is the velocity potential. Eq. (1) is known as the Laplace equation. The boundary conditions for this problem are the impermeability condition (zero normal velocity on a body) and the far field condition (the disturbance created by the motion should decay far from the body).

The Laplace equation has many possible analytic solutions and, being linear, the principle of superposition applies. Thus, if $\phi_1, \phi_2, ..., \phi_n$ are solutions of the equations, then

$$\phi = \sum_{k=1}^{n} c_k \phi_k \tag{2}$$

is also a solution and $c_1, c_2, ..., c_n$ are arbitrary constants. The solutions used by this computational model are the source and doublet, located at (x_0, y_0, z_0) in the Cartesian system, and given respectively by

$$\phi = -\frac{\sigma}{4\pi\sqrt{(x-x_0)^2 + (y-y_0)^2 + (z-z_0)^2}} \tag{3}$$

and

$$\phi = \frac{\mu}{4\pi} \begin{Bmatrix} \frac{\partial}{\partial x} \\ \frac{\partial}{\partial y} \\ \frac{\partial}{\partial z} \end{Bmatrix} \frac{1}{\sqrt{(x-x_0)^2 + (y-y_0)^2 + (z-z_0)^2}}\,, \tag{4}$$

where σ and μ are the source and doublet strength, respectively.

2.2. Panel Method

Given the pertinent solutions for the Laplace equation, the CFD model employs a numerical panel method based on the formulation from Katz and Plotkin [2] to solve the problem. The objective is to find the strength of the singularity elements distributed on the body surface and, consequently, to compute the velocity and pressure distribution.

Based on Green's identity and applying the Dirichlet boundary condition, Eq.(1) can be developed by a sum of source and doublet distributions on the boundary of the body and the wake, yielding

$$\begin{aligned} &\frac{1}{4\pi} \int_{body+wake} \mu \vec{n} \cdot \frac{\partial}{\partial n} \left(\frac{1}{r}\right) dS \\ &- \frac{1}{4\pi} \int_{body} \sigma \left(\frac{1}{r}\right) dS = 0\,. \end{aligned} \tag{5}$$

The source strength is required to be $\sigma = \vec{Q}_\infty \cdot \vec{n}$, where $\vec{Q}_\infty$ is the free-stream velocity vector.

The wake doublet strength comes from the Kutta condition in terms of the doublet strength at the trailing-edge. As a result, μ is constant in the wake (μ_w) and is equal to the value at the trailing-edge (μ_{TE}), resulting in

$$\mu_w = const. = \mu_{TE} \leftrightarrow \mu_U - \mu_L = \mu_w\,, \tag{6}$$

where μ_U and μ_L are, respectively, the upper and lower surface doublet strengths at the trailing edge.

To obtain a solution for the problem, the body surface is divided into N surface panels and N_W additional wake rectilinear panels, each one assumed to have constant strength. This problem is then reduced to a set of linear algebraic equations

$$\sum_{k=1}^{N} C_k \mu_k + \sum_{l=1}^{N_W} C_l \mu_l + \sum_{k=1}^{N} B_k \sigma_k = 0\,, \tag{7}$$

where for each collocation point the summation of the influences of all k body panels and l wake panels is needed. The influence of a panel on a collocation point depends only on the panel geometry. Once the strengths of each panel are calculated, the two

tangential and normal velocity components are, respectively,

$$V_l = -\frac{\partial \mu}{\partial l}, \quad V_m = -\frac{\partial \mu}{\partial m}, \quad V_n = -\sigma\,, \qquad (8)$$

where (l, m, n) are the local coordinates of the panel being n normal to the panel. The total velocity on panel k becomes

$$\vec{V_k} = (V_{\infty l}, V_{\infty m}, V_{\infty n})_k + (V_l, V_m, V_n)_k\,. \qquad (9)$$

In an unsteady case, the wake shape is obtained using a time-stepping method. Therefore, the wake is directly related to the motion, being convected with $\vec{V}_\infty$ at each time step.

To compute the pressure distribution, the Bernoulli equation for inviscid, incompressible and irrotational flow will be used,

$$\frac{p_{ref} - p}{\rho} = \frac{V^2}{2} - \frac{v_{ref}^2}{2} + \frac{\partial \phi}{\partial t}\,. \qquad (10)$$

Considering the infinity as the point of reference, the pressure coefficient can be calculated from

$$C_p = \frac{p - p_\infty}{0.5\rho V_\infty^2} = 1 - \left(\frac{V}{V_\infty}\right)^2 - \frac{2}{V_\infty^2}\frac{\partial \phi}{\partial t}\,. \qquad (11)$$

In order to solve Eq.(11) in time, a time discretization method is needed. An implicit method is required, as the objective is to obtain the pressure coefficient at time $t + \Delta t$. The largely used option is the Backward Euler Method. Applied to Eq.(11) yields

$$C_p^{t+\Delta t} = 1 - \frac{(V^{t+\Delta t})^2}{V_\infty^2} - \frac{2}{V_\infty^2}\left(\frac{\phi^{t+\Delta t} - \phi^t}{\Delta t}\right)\,, \qquad (12)$$

which is first-order accurate.

2.3. Implementation

In order to validate the results obtained by this program [4] (named Cardeira for reference), a steady aerodynamic analysis of a rectangular wing is employed. The results are compared with numerical and experimental results of a similar panel method developed by Baltazar [5]. To have the same conditions, a mesh of 64x32 panels is used. The plots in Figure 2 represent the pressure distributions in specific spanwise sections of the wing, with $AR = 4$ and NACA 0015 airfoil, for angle of attack of 2.5°. It can be concluded that the results from both programs are very similar. Moreover, these figures show a good approximation between the numerical and experimental results, even at the wing tip.

In order to evaluate the results with the mesh refinement, a rectangular wing with NACA 0010 airfoil, $AR = 4$, $b/2 = 2m$ and $c = 1m$ is evaluated at $\alpha = 6°$. Table 1 presents the values of lift and drag coefficients for different meshes, which are compared between the two programs.

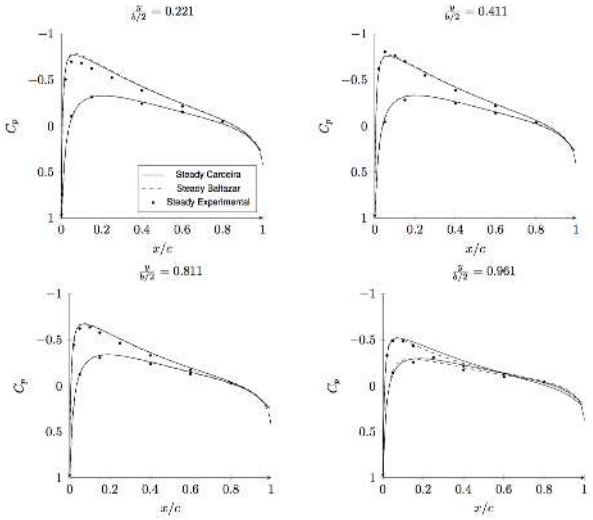

Figure 2: Pressure distributions for specific spanwise locations, with 64x32 panels and $\alpha = 2.5°$.

Mesh	Steady Cardeira		Steady Baltazar	
	C_L	C_D	C_L	C_D
16x10	0.0884	0.0038	0.1082	0.0039
32x18	0.0940	0.0064	0.1024	0.0034
64x34	0.0959	0.0074	0.1002	0.0032
128x66	0.0965	0.0079	0.0993	0.0031

Table 1: Steady lift and drag coefficient results comparison for different mesh sizes.

It is concluded that, with an increasing mesh refinement, the values of C_L are approximated from Steady Cardeira to Steady Baltazar, while the opposite occurs regarding C_D. However, the values of drag are not so relevant for aeroelastic analysis as the lift, not only because they are much lower but also due to the pitching movement of the wing being mainly caused by the action of the lift forces.

3. Structural Dynamics Model

The development of a computational structural dynamics model used to perform aeroelastic calculations is one of the main objectives of this thesis. It is based on a finite element approach describing an equivalent aircraft wing beam model.

3.1. Beam Element Formulation

The structure of the wing is modeled as a linear finite element structure that can undergo bending and torsion, with all rigidity concentrated at the nodes. This model has lower complexity and lower computational cost than higher fidelity models. However, these factors are crucial in the preliminary design stages and optimization, increasing

computational efficiency while capturing the most important structural responses.

To model the wing as an equivalent beam, a 3D beam element was selected, as illustrated in Figure 3. This element has 2 nodes and 6 degrees of freedom per node: 3 translational and 3 rotational degrees of freedom. The element formulation is based on Euler-Bernoulli beam theory [6], which means the cross-sections remain rigid, thereby uncoupling the bending and torsional displacements. This approach is suitable for long beams such as high aspect-ratio wings, neglecting the shear deformations of the cross-section.

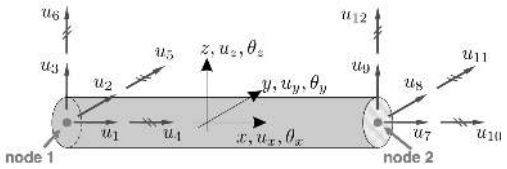

Figure 3: 3D beam element.

This element is composed of 4 sub-elements:

- 1 bar element subjected only to axial forces resulting in axial deformation given by

$$\frac{d}{dx}\left(EA\frac{du_x}{dx}\right) + b(x) = 0\,, \tag{13}$$

  where A is the area of the beam cross-section, E is the Young's modulus of the material, u_x is the axial displacement along the x axis and $b(x)$ is the axial applied force per unit length;

- 1 torsion element subjected to a twisting load resulting in the free torsion equation

$$\frac{d}{dx}\left(GJ\frac{d\theta_x}{dx}\right) + m_x = 0\,, \tag{14}$$

  where G is the shear modulus of the material, J is the torsional moment of inertia, θ_x is the torsion and m_x is the distributed twisting load;

- 2 elements with translational and rotational deformation in the xz and xy planes subjected to shear forces and moments, resulting in the bending equation

$$\frac{d^2}{dx}\left(EI_{yy/zz}\frac{d^2u_{z/y}}{dx^2}\right) - q(x) = 0\,, \tag{15}$$

  where $I_{yy/zz}$ is the area moment of inertia about the y/z axis, $u_{z/y}$ is the vertical/horizontal displacement and $q(x)$ is a distributed force in the z/y direction along the x axis.

The finite element approach used in this work is based on the formulation from Reddy [6] and Cook et al. [7]. In order to compute the element stiffness and mass matrices, shape functions are necessary. These functions relate the displacement field for the beam, i.e., the axial displacement $u_x(x)$, deflections $u_y(x)$ and $u_z(x)$ and angle of twist $\theta_x(x)$, with the nodal values of these quantities. Linear shape functions were used for the axial displacement and torsion whereas cubic shape functions were used for the transverse displacement. In the end, the shape functions can be disposed in matrix form as

$$\{u\} = [N]\{d\}\,, \tag{16}$$

where u is the vector of displacements, N is the matrix with the shape functions and d is the vector of nodal displacements.

A formal procedure will be followed to formulate the element stiffness and mass matrices, based on potential and kinetic energy. The strain vector for this element includes axial strain, curvatures and twist angle which can be computed by

$$\begin{Bmatrix}\epsilon_x\\ \kappa_z\\ \kappa_y\\ \theta_x\end{Bmatrix} = \begin{bmatrix}\frac{\partial}{\partial x} & 0 & 0 & 0\\ 0 & \frac{\partial^2}{\partial x^2} & 0 & 0\\ 0 & 0 & \frac{\partial^2}{\partial x^2} & 0\\ 0 & 0 & 0 & \frac{\partial}{\partial x}\end{bmatrix}[N]\{d\} = [B]\{d\}\,, \tag{17}$$

where B is the strain-displacement matrix. For isotropic materials, the axial force, bending moment in the two symmetric planes and torsional moment are given by

$$\begin{Bmatrix}N_x\\ M_z\\ M_y\\ M_x\end{Bmatrix} = \begin{bmatrix}EA & 0 & 0 & 0\\ 0 & EI_{zz} & 0 & 0\\ 0 & 0 & EI_{yy} & 0\\ 0 & 0 & 0 & GJ\end{bmatrix}\begin{Bmatrix}\epsilon_x\\ \kappa_z\\ \kappa_y\\ \theta_x\end{Bmatrix} = [D]\{\epsilon\}\,, \tag{18}$$

where N_x is the axial force along the x axis and (M_x, M_y, M_z) are the components of the bending and torsion moments.

The potential energy of the finite element is given by

$$\begin{aligned}V = &\frac{1}{2}\{d\}^T\int_\Omega [B]^T[D][B]d\Omega\{d\}\\ &-\{d\}^T\int_\Omega [N]^T\{F_v\}d\Omega - \{d\}^T\int_S [N]^T\{F_s\}dS\,,\end{aligned} \tag{19}$$

where Ω and S are, respectively, the element domain and surface, $\{F_v\}$ and $\{F_s\}$ represent the volume and surface forces, respectively and $[K]_e$ is the stiffness matrix of the element, with the property of being symmetric, given by

$$[K]_e = \int_\Omega [B]^T[D][B]d\Omega\,. \tag{20}$$

While the stiffness matrix accounts for the elastic deformation, it is still necessary to consider the in-

ertial properties of the element for a dynamic structural analysis. This is done by considering the kinetic energy of the finite element, given by

$$T = \frac{1}{2}\{\dot{d}\}^T \int_\Omega \rho[N]^T[N]d\Omega\{\dot{d}\}\,, \tag{21}$$

where ρ is the material density of the element and $[M]_e$ is the mass matrix of the element, which is a symmetric matrix, given by

$$[M]_e = \int_\Omega \rho[N]^T[N]d\Omega\,. \tag{22}$$

3.2. Computation of Cross-Section Properties

In order to compute the cross-section properties of the wing, that is, the axial stiffness EA, the bending stiffness EI_{yy}, the bending stiffness EI_{zz} and the torsional stiffness GJ, applied in the element stiffness and mass matrices, a mathematical model was developed. The several steps conducted are:

- Discretize cross-section into area segments: upper and lower surfaces and shear webs are discretized into many segments;
- Calculate area moments of inertia of each area segment;
- Calculate shear center of the cross-section, the point through which shear loads produce no twisting;
- Transfer the area moments of inertia of each area segment to elastic axis (origin at shear center);
- Sum contributions of all area segments to determine axial and bending stiffness;
- Determine torsional stiffness with Bradt-Batho Shear Flow Theory (BSFT) [8];
- Calculate Von Mises equivalent stress and output results.

3.3. Implementation

The CSD model was implemented in Matlab® language due to its strong matrix manipulation and useful plotting tools. The input parameters needed for the finite element analysis are:

- The number and coordinates of nodes in terms of the global coordinate system;
- The cross-section properties, *e.g.*, total area and moments of inertia;
- The material properties, *e.g.*, Young modulus, shear modulus and density;
- Information for boundary conditions;
- The nodal forces relative to the global coordinate system.

The elements are computed with the coordinates of their nodes. A mesh with n elements has $n+1$ nodes. Once the matrices are computed for each element, they need to be assembled in the global stiffness and mass matrices. In the end, a global matrix is obtained whose size is equal to the total number of degrees of freedom in the system (6 times the number of nodes).

Without applying constraints to the system of global equations, the matrices are singular and so they cannot be inverted in order to solve the static and dynamic problems. To overcome this, boundary conditions must be applied to one or more degrees of freedom in the stiffness and mass matrices. For example, a beam with a fixed support at one of its ends, must have the first 6 degrees of freedom nullified. These constitute the primary boundary conditions. The secondary boundary conditions are related to the loads applied on the structure, which must be located on its nodes. Each node, in turn, requires three forces and three moments. As a result, at each element the loads are inserted into a vector F, whose components are the applied forces and moments at each node. In the end, each element load vector must be assembled into a global load vector in order to match the global stiffness and mass matrices ordering.

When analyzing the solution of a static or dynamic analysis, it is useful to obtain displacements and rotations in the global coordinate system. The element coordinates are related to the global coordinates by

$$\{d_l\} = [T_R]\{d\}\,, \tag{23}$$

where d_l is the vector of displacements in element Cartesian coordinates, d is the vector of displacements in global Cartesian coordinates and T_R is called the *transformation or rotation matrix*. In the end, the element stiffness and mass matrices in global coordinates become

$$[K] = [T_R]^T[K_l][T_R]\,, \tag{24}$$

$$[M] = [T_R]^T[M_l][T_R]\,. \tag{25}$$

3.4. CSD Program Validation

A first static linear analysis was performed and the results compared with results from ANSYS® APDL, using BEAM4 elements matching the beam element implemented in this thesis. For this, a rectangular aluminum beam with $EA = 1.4E9\ N$, $EI_{yy} = 1.17E6\ N.m^2$, $EI_{zz} = 4.67E6\ N.m^2$, $GJ = 2.241E6\ N.m^2$, $\rho = 2700\ Kg.m^{-3}$ and a length $L = 10\ m$ was selected.

To study the convergence of the tip displacement of the cantilever beam with mesh refinement, the

beam is subjected to an applied force $F_z = 1000N$ at the tip, in the positive z direction. The results obtained are present in Table 2. As it can be seen, the displacements converge very fast for both analyses and the results are the same.

Elem.	1	10	100	1000	2000
Matlab®	0.286	0.286	0.286	0.286	0.286
ANSYS®	0.286	0.286	0.286	0.286	0.286
Difference (%)	0.000	0.000	0.000	0.000	0.000

Table 2: Convergence study of beam tip vertical displacement and comparison with ANSYS® APDL.

The same beam was used to perform a transient analysis with the Newmark time-integration method choosing a time step size of 0.001 s and 10 finite elements. A load case with $F_z = 1000N$ and $M_x = 1000N.m$ applied at the tip is tested. Figures 4(a) and 4(b) represent the transient response of the beam subjected to the load case chosen. A comparison with results from ANSYS® APDL, using element type BEAM4, was employed. It can be concluded that the vertical displacement results were perfectly matched in both cases. On the other hand, the torsional rotation results present a slight deviation. However, the frequency and mean value are identical.

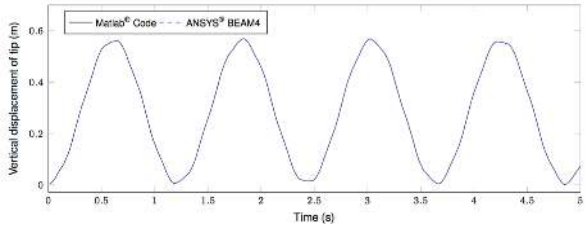

(a) Vertical displacement of beam tip node.

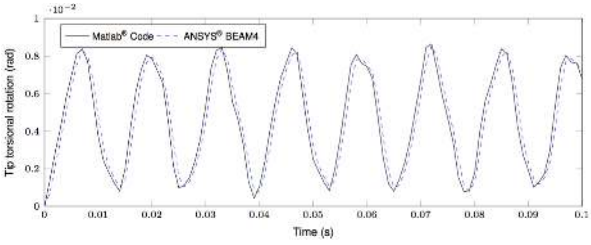

(b) Torsional rotation of beam tip node.

Figure 4: CSD transient numerical results and comparison with ANSYS® APDL.

Finally, a modal analysis was performed and the results were used to validate the structural model. For this, a prototype high aspect ratio wing that has been extensively reported in the literature, and is present in the paper from Patil et al. [9], is modeled. The author presents exact results for frequencies of an equivalent beam with torsion, flapwise bending and chordwise bending. Therefore, the first five natural frequencies were extracted and compared with the same ones obtained in Table 3 in SI units. All frequencies are very similar with relative differences below 1%. Adding the good results from the previous analyses, it is concluded that the structural model developed is accurate enough to perform aeroelastic analyses.

	Matlab®	**[9]**	**Difference (%)**
1^{st} flap.	2.243	2.243	0.000
2^{nd} flap.	14.057	14.056	0.007
3^{rd} flap.	39.369	39.356	0.033
1^{st} torsion	31.081	31.046	0.113
1^{st} chord.	31.727	31.718	0.028

Table 3: Equivalent beam first five natural frequencies (in rad/s) calculated with developed code and compared to results from [9].

4. Fluid-Structure Interaction

Fluid-Structure Interaction (FSI) deals with the coupling and interaction between the fluid and structural domains. The range of FSI models can be divided in monolithic and staggered categories. In this work, only staggered algorithms will be studied.

4.1. Staggered Coupling Methods

The most basic staggered method is referred to as the *Conventional Serial Staggered* (CSS) procedure in [10] and it is outlined in Figure 5, where u is the structure state vector (nodal displacements), w denotes the fluid state vector, p represents the fluid pressure, x is the fluid grid position, the subscript n designates the n^{th} time step, and the equalities shown at the top hold on the fluid/structure interface boundary.

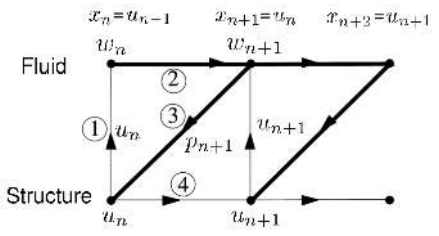

Figure 5: Conventional Serial Staggered (CSS) procedure [10].

One possible enhancement for this method is to subcycle the fluid computations, reducing the overall number of structural integrations. The algorithm is identical to the CSS, where the difference

resides in the number of fluid subcycles used, which is given by

$$n_{S/F} = \frac{\Delta t_S}{\Delta t_F} \tag{26}$$

where Δt_S and Δt_F are, respectively, the structure and fluid time steps.

Unlike the CSS, another possible methodology is to use a structural predictor. This methodology, unlike the CSS, does not require that the fluid and the structural boundaries are matching after each time step. Therefore, a prediction for the global state of the structure after a time step is introduced and the fluid is time-integrated, assuming the fluid grid is matching the location of the structure that was predicted. At the end of a time step, continuity of the structural and fluid grid displacements at the interface is *a priori* not satisfied unless the structural predictor is perfect. The use of subiterations aims to remedy this aspect, where each block of Figure 5 is repeated until convergence is achieved. Two types of predictors were implemented, a linear first-order and a second-order accurate given, respectively, by

$$\tilde{u}^{n+1} = u^n + \Delta t_S \dot{u}^n \,, \tag{27}$$

$$\tilde{u}^{n+1} = u^n + \Delta t_S (1.5\dot{u}^n - 0.5\dot{u}^{n-1}) \,. \tag{28}$$

Another alternative method is presented in [10], which predicts the structural displacement at the middle of each time step, and is referred as the *Improved Serial Staggered Algorithm* (ISS).

4.2. Implementation

The structural nodes are located at the middle and at the limits of each ring of panels of the fluid grid, as shown in Figure 6. This option is justified with the necessity of mapping the fluid forces computed at the middle of the panels to the structural nodes, hence the position of the nodes at the middle of the ring, and the necessity of extrapolating the structural displacements to the CFD grid points, which corresponds to the panel corner points, hence the position of the nodes at the sides of each ring. Concerning these last nodes, their only role is to transfer the displacement to the CFD grid points. Thereby, no nodal forces are applied on them.

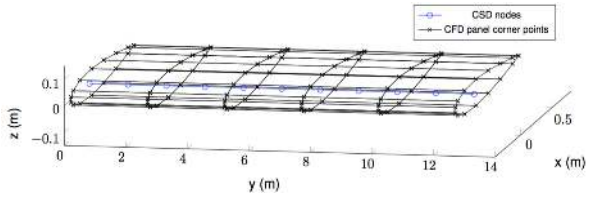

Figure 6: CFD and CSD grids.

Assuming the pressure is constant at each panel, the forces at each collocation point are calculated and an orientation vector is computed to seek the components of the force vector in the global reference system. Then, these components are mapped to the structural nodes by an equivalent force system as *D'Alembert's Principle* requires.

In order to update the CFD grid at every time step, a linear extrapolation procedure was employed to transfer the displacements of the beam model to the original CFD grid, resulting in the new CFD surface mesh. The new positions of the CFD grid were obtained assuming a rigid link connection between the structural nodes positioned at the limits of each ring of panels and the respective panel corner points. The links are assumed to be perpendicular to the elastic axis of the wing. The displacement of a CFD panel corner point can be separated into three components: a translation component u_z, a translation component u_x and a rotation component θ_y. Figure 7 demonstrates this procedure. The

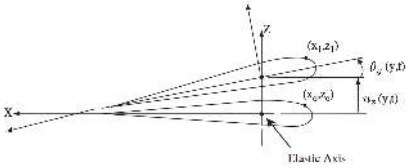

Figure 7: Extrapolation procedure.

subscript 0 denotes the original location of the CFD grid panel corner points while the subscript 1 denotes the new location. Obtaining the structural solution and knowing the values of u_z, u_x and θ_y at each location on the spanwise direction and at each time step, the new location is obtained by

$$x_1 = x_0 cos(\theta_y) + z_0 sin(\theta_y) + u_x \,, \tag{29}$$

$$z_1 = z_0 cos(\theta_y) - x_0 sin(\theta_y) + u_z \,. \tag{30}$$

To validate this extrapolation and the transferring of the forces from the fluid to the structure grid, a static analysis was conducted and validated with results from [11]. In that paper, the static deformation of a wing with angle of attack 10° is calculated when subjected to a free-stream velocity of 25 m/s. Figure 8 illustrates the results computed with the developed code and the paper results. Despite the different aerodynamic model used to achieve the aeroelastic solution, the results are very close.

5. Results

The created aeroelastic framework was used to perform a benchmark of the FSI staggered algorithms, a parametric study and an aero-structural optimization.

5.1. Reference Input Data

A rectangular wing with a NACA0015 airfoil, chord of 1 m, semi-span of 7 m and 2° angle of attack was

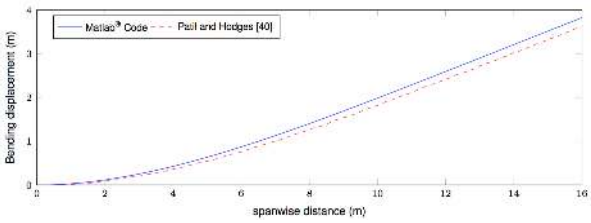

Figure 8: Wing static bending displacement at 25 m/s and angle of attack 10°.

selected as the reference case. The wing is made of a single material (aluminum skin and spars) with properties $E = 75$ GPa, $G = 30$ GPa and $\rho = 2800$ kg/m^3. The internal structure is composed of two spars which go from the root to the tip, placed at 30% and 70% of the chord, respectively, with 1 cm of thickness. The wing skin thickness is 5 mm. The root of the wing is fixed, simulating the place where it is attached to the fuselage of the aircraft. It is subjected to a free stream velocity of 75 m/s and the fluid density is assumed to be $\rho = 1$ kg/m^3 corresponding to an altitude of 1371 m at standard atmosphere conditions (considering a temperature offset of 20 ^oC). For the sake of efficiency, a coarse grid of 20x10 panels is chosen and a time step size of 0.1 s for the structural solver is selected.

5.2. Benchmark of FSI Staggered Algorithms

The algorithms used for comparison are: CSS1: *Conventional Serial Staggered Algorithm*; CSS2: *Serial Staggered Algorithm with First Order Structural Predictor*; CSS3: *Serial Staggered Algorithm with Second Order Structural Predictor* and CSS4: *Improved Serial Staggered Algorithm.*

The first tests aim to study the influence of subiterating the CSS2 and CSS3 algorithms. Different analyses were conducted in order to study the behavior of the aeroelastic response of the wing. However, the results are practically not affected by the use of subiterations, which suggests the predictors give a good approximation of the displacement at the end of each time step. Since the computational time increases linearly with the amount of subiterations used, it is not advantageous to use them.

The following tests are relative to the influence of subcycling the fluid solver. The main advantage of using subcycles is the possibility of having a small enough time step size for the fluid solver, while having a larger time step for the structural solver. This way, efficiency is obtained while preserving accuracy. The different analyses conducted are shown in Figure 9.

It can be concluded that increasing the number of subcycles also increase the maximum displacement in the negative direction while slightly decreasing the maximum displacement in the positive direction. This aspect is valid for every staggered algorithm tested. However, the stability of the movement remains unchanged while varying the number of subcycles. For example, in every analysis performed, the behavior from CSS1 is stable while the behavior from CSS3 is divergent, being already beyond the flutter velocity.

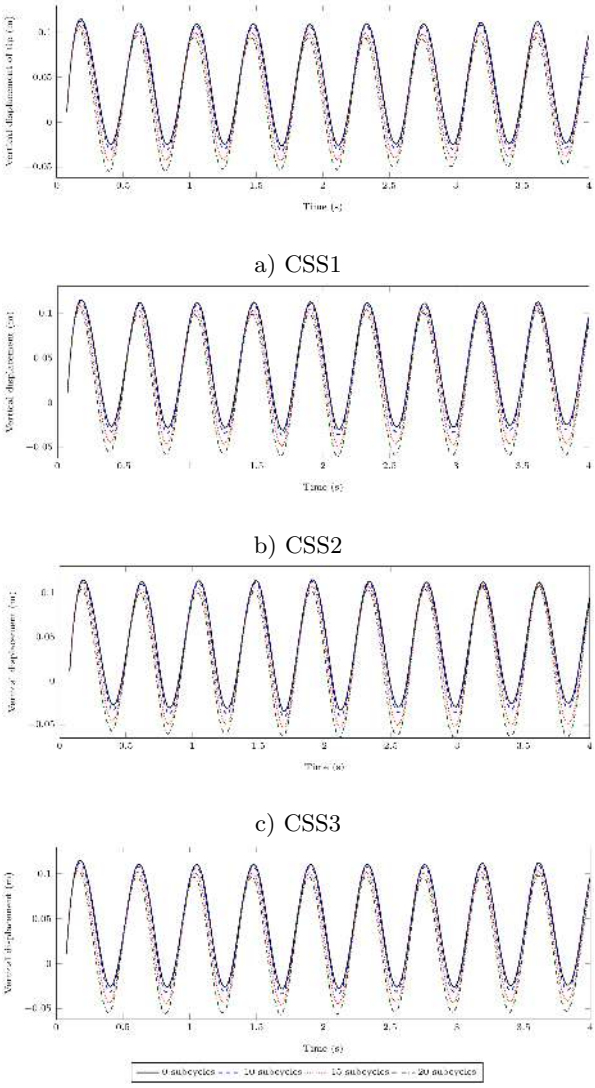

a) CSS1

b) CSS2

c) CSS3

d) CSS4

Figure 9: Influence of subcycling in the aeroelastic wing behavior.

Figure 10 makes this aspect more clear. Both the CSS1 and CSS4 algorithms predict a stable behavior of the wing unlike the CSS2 and CSS3 algorithms. The most divergent movement occurs when employing the CSS3 algorithm, which uses a second-order predictor in contrast to the first-order predictor used by the CSS2 algorithm.

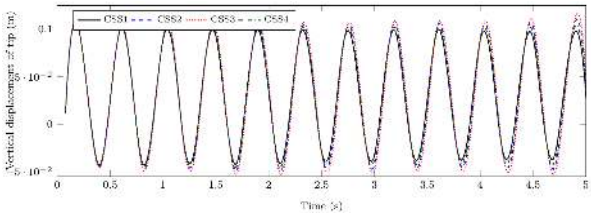

Figure 10: Comparison of the tip velocity displacement, using 15 subcycles and no subiterations.

5.3. Aeroelastic Parametric Study

This study will be focused on the bending movement of the wing using the reference input data and changing one parameter at a time. Only some of the parameters studied will be presented here, namely, the free-stream velocity, sweep angle, spars thickness, material density and Young modulus. The results are plotted and compared to the reference case in Figure 11.

Overall, the study revealed results which are in very good agreement to the theoretical influences of the parameters studied.

5.4. Aero-structural Optimization

The constrained optimization problem conducted can be formulated as

$$\begin{aligned} \underset{\vec{x}}{\text{minimize}} \quad & f(\vec{x}) = WingMass \\ \text{subject to} \quad & C_L = 0.04, \sigma_{VM} \leq 270MPa, \delta_{tip} \leq 0.7m\,, \end{aligned}$$

where $\vec{x}$ is a vector containing 10 design variables: taper ratio λ, sweep angle Λ, dihedral angle Γ, twist angle at tip θ_{tip}, angle of attack α, front and rear spars location $x_{spar,f}$ and $x_{spar,r}$, spars and skin thicknesses t_{spars} and t_{skin}. Table 4 lists the chosen variables lower and upper bounds, as well as the initial and optimal values.

Parameter	Lower bound	Upper bound	Initial	Optimal
λ	0.3	1	1	0.3 (min)
Λ (°)	0	10	0	0 (min)
Γ (°)	0	10	0	0.05
θ_{tip} (°)	0	10	0	3
α (°)	1	10	2	3.8
$x_{spar,f}$ (%)	10	40	30	10 (min)
$x_{spar,r}$ (%)	50	90	70	90 (max)
t_{spars} (m)	0.01	0.05	0.01	0.01 (min)
t_{skin} (m)	0.001	0.01	0.005	0.001 (min)

Table 4: Design variables: bounds and optimal values.

In order to satisfy the constraint related to the lift coefficient, the wing angle of attack and twist angle increase, mainly because the taper ratio decreases and, consequently, the wing surface area does too. As a result, the lift generated must be higher, which is provided by the change in those parameters. Since the objective was to minimize the total mass, the taper ratio decreases while the thicknesses diminish. Finally, it is concluded that some of the optimal values are either in the predefined lower or upper bounds, as shown in Table 4. This may indicate that the solution is not properly constrained. In fact, the solution is not tip deflection constrained nor stress constrained since the optimal values of

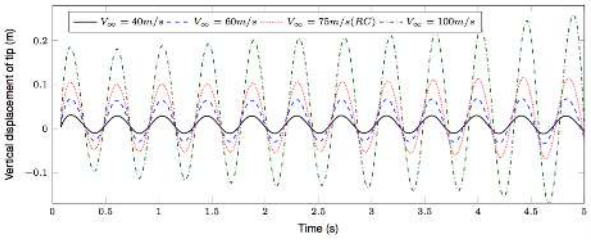

a) Influence of free stream velocity.

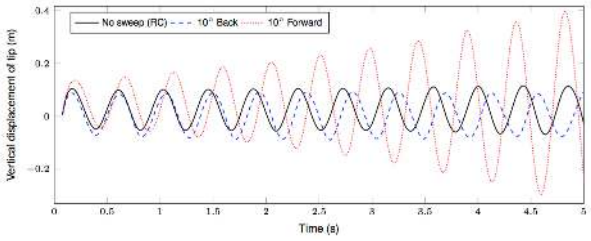

b) Influence of sweep angle.

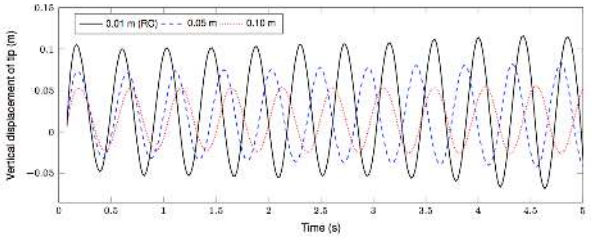

c) Influence of spar thickness.

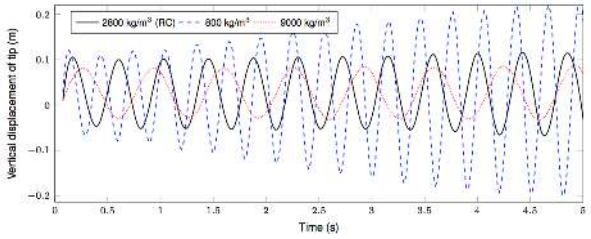

d) Influence of material density.

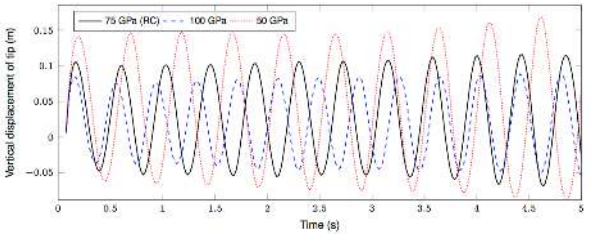

e) Influence of Young modulus.

Figure 11: Parametric study.

these properties are much lower than the respective bounds: $\delta_{tip,optimal} = 0.23m < \delta_{tip,max} = 0.7m$ and $\sigma_{optimal} = 72MPa << \sigma_{max} = 270MPa$.

It is concluded that the wing is still very rigid and the optimal thicknesses, which are already in the lower bound limit, could be smaller since the objective is to reduce the wing mass. However, the bounds must be chosen carefully as a too low value could lead to a solution failing to meet other constraints. It should be noticed that no buckling effects were considered in the analysis. Had this been done, possibly a different optimal thickness would have resulted.

Finally, it is shown that C_L converges to the desired value, being the only constraint that is fully met.

6. Conclusions

A computational tool was developed with the purpose of studying the aerolelastic behavior of a 3D aircraft wing. It comprises three main parts: a fluid model based on panel method, a structural model based on beam element formulation and a coupling procedure.

The aerodynamics were modeled according to potential fluid theory in which the pressure forces were calculated based on a panel method. The structural model consisted of a one-dimensional beam clamped at the aircraft fuselage, and representative of the wing elastic axis. The coupling of the fluid and structural models was a crucial part of this work. The equivalent beam was placed inside the wing and a linear extrapolation procedure was employed to transfer the displacements of the beam model to the original fluid grid, assuming a rigid link connection between the structural nodes and the fluid grid points.

Several coupling algorithms were taken from the literature and presented, before being implemented and tested. After studying the effect of these algorithms on the aeroelastic results of a reference case wing, it was concluded that the use of subcyles has a major impact on the amplitude of the movement but does not change its stability while the use of subiterations do not have any significant impact. Furthermore, when using a structural predictor, the movement becomes divergent. Additionally, a parametric study was conducted with one of these algorithms. All tests revealed results which were physically correct.

Finally, a simple aero-structural optimization case study was conducted. The objective was to minimize the wing mass while constraining the tip deflection, maximum stress and lift coefficient.

An important step for future work would be to construct a wing model to perform tests in a wind tunnel to validate the aeroelastic results computed with this framework.

References

[1] R. Clark, D. Cox, H. C. Curtiss Jr., J. W. Edwards, K. C. Hall, D. A. Peters, R. Scanlan, E. Simiu, F. Sisto, and T. W. Strganac. *A Modern Course in Aeroelasticity*, volume 116 of *Solid Mechanics and its Applications*. Kluwer Academic Publishers, 4th edition, 2005. ISBN: 9781402020391.

[2] J. Katz and A. Plotkin. *Low-Speed Aerodynamics*. Cambridge University Press, New York, 2nd edition, 2001. ISBN: 9780521662192.

[3] A. S. Cardeira. Aeroelastic analysis of aircraft wings. *Instituto Superior Técnico (IST)*, December 2014. MSc dissertation.

[4] J. M. R. D. C. Baltazar. On the modelling of the potential flow about wings and marine propellers using a boundary element method. *Instituto Superior Técnico (IST)*, 2008. PhD dissertation.

[5] J. N. Reddy. *An Introduction To The Finite Element Method*. McGraw-Hill Series in Mechanical Engineering. McGraw-Hill, 3rd edition, 2006. ISBN: 0072466855.

[6] R. D. Cook, D. S. Malkus, M. E. Plesha, and R. J. Witt. *Concepts and Applications of Finite Element Analysis*. John Wiley & Sons. Inc, 4th edition, 2002. ISBN: 0471356050.

[7] T. H. G. Megson. *Aircraft Structures for Engineering Students*. Elsevier, 4th edition, 2007. ISBN: 0080969054.

[8] M. J. Patil, D. H. Hodges, and C. E. S. Cesnik. Nonlinear aeroelasticity and flight dynamics of high-altitude long-endurance aircraft. *Journal of Aircraft*, 38(1):88–94, 2001. DOI: 10.2514/2.2738.

[9] C. Farhat and M. Lesoinne. Two efficient staggered algorithms for the serial and parallel solution of three–dimensional nonlinear transient aeroelastic problems. *Computer Methods in Applied Mechanics and Engineering*, 182(3-4):499–515, 2000. DOI: 10.1016/S0045-7825(99)00206-6.

[10] M. J. Patil and D. H. Hodges. On the importance of aerodynamic and structural geometrical nonlinearities in aeroelastic behavior of high-aspect-ratio wings. *Journal of Fluid and Structures*, 19(7):905–915, August 2004. DOI: 10.1016/j.jfluidstructs.2004.04.012.